



## Forced Imbibition in Porous Media: A Fourfold Scenario

Céleste Odier,<sup>1,2</sup> Bertrand Levaché,<sup>2,3</sup> Enric Santanach-Carreras,<sup>2,3</sup> and Denis Bartolo<sup>1,\*</sup>

<sup>1</sup>Univ Lyon, Ens de Lyon, Univ Claude Bernard, CNRS, Laboratoire de Physique, F-69342 Lyon, France

<sup>2</sup>Total SA. Pôle d'Etudes et Recherche de Lacq, BP 47-64170 Lacq, France

<sup>3</sup>Laboratoire Physico-Chimie des Interfaces Complexes, Total-ESPCI Paris-CNRS-UPMC, BP 47-64170 Lacq, France

(Received 19 May 2017; revised manuscript received 6 September 2017; published 17 November 2017)

We establish a comprehensive description of the patterns formed when a wetting liquid displaces a viscous fluid confined in a porous medium. Building on model microfluidic experiments, we evidence four imbibition scenarios all yielding different large-scale morphologies. Combining high-resolution imaging and confocal microscopy, we show that they originate from two liquid-entrainment transitions and a Rayleigh-Plateau instability at the pore scale. Finally, we demonstrate and explain the long-time coarsening of the resulting patterns.

DOI: 10.1103/PhysRevLett.119.208005

About a hundred years ago field engineers noticed that water does not homogeneously displace oil confined in porous media [1]. After a century of intense research, our understanding of driven liquid interfaces remains surprisingly unbalanced. The case of drainage where the defending fluid wets the confining solid, is fairly well understood, and so is the spontaneous imbibition of a wetting liquid through dry porous structures, such as the rise of a coffee drop in a sugar cube [2–6]. In stark contrast, much less attention has been paid to the situation where imbibition is used to mobilize a more viscous liquid [3,7,8]. For more than twenty years, and despite its relevance to a number of industrial processes, our knowledge about forced imbibition has been mostly limited to a seminal phase diagram constructed by Lenormand from heuristic arguments [3]. However, recent microfluidic experiments [9–12], and simplified 2D simulations [13] have revisited this framework, and established the dramatic impact of wetting properties on liquid displacement. Nonetheless, we still lack a comprehensive picture of forced-imbibition patterns, and of the underlying interfacial dynamics at the pore scale.

In this Letter, we contribute to resolving this situation. Building on model microfluidic experiments, we first demonstrate four classes of macroscopic imbibition patterns yielding nonmonotonic variations of the recovery rate with the driving strength. We then show that they stem from four types of microscopic interfacial dynamics separated by two film-entrainment transitions and one interfacial. Finally, we evidence and explain the long-time coarsening of the resulting macroscopic patterns.

Our experiment consists of injecting an aqueous liquid in a hydrophilic porous medium filled with viscous oil; see the Supplemental Material, movie 1 [14]. Details about the materials, the channel geometry, the microfluidic and imaging methods are provided in the Supplemental Material, document [14]. In brief, we use a simplified 2D rectilinear geometry consisting of a rectangular hydrophilic

microfluidic sticker including a square lattice of posts forming interconnected channels of dimensions  $200\ \mu\text{m} \times 80\ \mu\text{m} \times 70\ \mu\text{m}$ , see Figs. 1(a) and Refs. [15,16]. We first fill the channels with a mixture of silicon oils. Oil is then displaced in this rectilinear displacement geometry by injecting an aqueous solution of dye and SDS (1 wt%) at a constant flow rate  $Q$ . Both the surface tension between the two liquids and the advancing contact angles of water on the solid substrates do not depend on the oil molecular weight. We find  $\gamma = 13 \pm 2\ \text{mN/m}$ , and  $\theta_A = 30 \pm 2^\circ$  ( $\theta_A = 20 \pm 2^\circ$ ) on the treated quartz (sticker) surface. The imbibition patterns are observed with a spatial resolution of  $11\ \mu\text{m}/\text{pixel}$ . The local thickness of the water films is measured from the transmitted-light intensity with an absolute precision of  $4\ \mu\text{m}$ , and with a precision of  $1\ \mu\text{m}$  on its temporal variations [9,14]. In addition, 3D reconstructions of the liquid interfaces at the pore scale are achieved in separate experiments using confocal microscopy.

Let us first discuss the impact of flow rate on the macroscopic pattern morphologies, while keeping constant both the wetting contact angles and the viscosity ratio, here  $M \equiv \eta_{\text{oil}}/\eta_{\text{water}} = 560$ . A natural dimensionless control parameter is given by the capillary number  $\text{Ca} = \eta_{\text{water}}Q/(\gamma S)$ , where  $S$  is the cross-section area of the microchannels separating the posts. Varying  $\text{Ca}$ , we observe four types of patterns exemplified in Figs. 1(a), and Supplemental Material, movie 1 [14]:

*Regime A.*—When  $\text{Ca} < 2.3 \times 10^{-5}$ , the patterns are typical of cooperative pore filling [17] yielding compact capillary domains [3]. A single macroscopic finger proceeds at constant speed, and its faceted edges reflect the square geometry of the underlying periodic lattice [18,19].

*Regime B.*—Increasing the flow rate,  $2.3 \times 10^{-5} < \text{Ca} < 9.1 \times 10^{-5}$ , we still observe the growth of a single yet narrower finger. However, the dynamics of the water-oil interface does not reduce to the motion of a stable meniscus. Instead, the spatial fluctuations of the transmitted

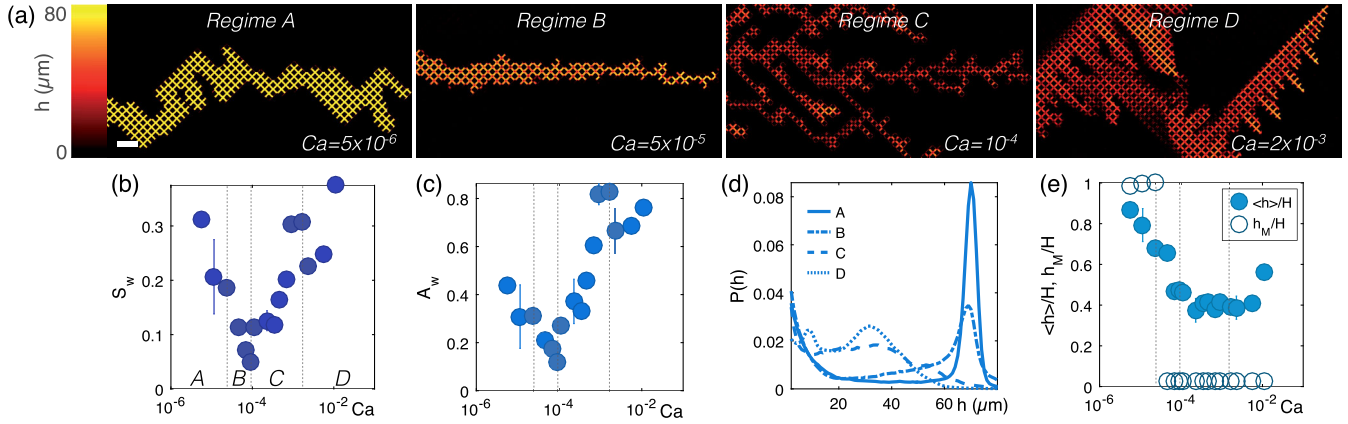


FIG. 1. Imbibition patterns. (a) Four imbibition patterns corresponding to the four regimes discussed in the main text. An aqueous solution is driven through a periodic lattice of channels filled with silicon oil ( $M = 560$ ). The color indicates the local thickness of the water films. Scale bar: 1 mm. (b) Variations of the water saturation with  $Ca$ . (c) Variations of the wetted area fraction with  $Ca$ . (d) Probability distribution of the local water-film thickness for the four capillary numbers corresponding to the experiments shown in (a). The distribution is computed from local thicknesses larger than  $2 \mu\text{m}$ . (e) Light blue circles: thickness of the water films averaged over the wetted region  $\langle h \rangle$  normalized by the average height of the microchannels  $H$ . Dark blue: most probable film thickness,  $h_M$  normalized by  $H$ . Error bars: maximum deviation from the mean (correspond to experiments repeated at least four times). The dashed vertical lines separate the four imbibition regimes.

light indicate that thin water films form and propagate throughout the lattice.

*Regime C.*—Further increasing the flow rate,  $9.1 \times 10^{-5} < Ca < 1.6 \times 10^{-3}$ , the patterns evolve into even thinner films forming patterns with multiple branches and reconnections. We emphasize that this geometry including branch reconnections qualitatively differs from typical viscous fingering motifs, and from all instances of Laplacian growth patterns [5].

*Regime D.*—Finally when  $Ca > 1.6 \times 10^{-3}$ , water films self-organize into nonintersecting branched patterns. They are reminiscent of dendritic growth and drainage dynamics [20–22]. Pushing the flow rate to even higher values yields the fragmentation of the oil-water interfaces, and to the formation of both direct and inverse emulsions.

These four dynamical regimes do not display any sign of metastability upon sudden changes in  $Q$  [14], and have a clear signature on four global observables. In Fig. 1(b) we show the variations of the water saturation  $S_w$  defined as the volume fraction of water, or, equivalently, as the fraction of oil extracted from the porous medium when the water front reaches the end of the device.  $S_w$  undergoes nonmonotonic variations with  $Ca$ , it reaches a minimum exactly at the transition between regimes  $B$  and  $C$ . Surprisingly, at small flow rates pushing faster hinders oil extraction.  $S_w$  also display a local maximum followed by a sharp drop at the transition between regimes  $C$  and  $D$ .

Ignoring the heterogeneities of the water-film thickness, the area fraction of the porous medium in contact with water,  $A_w$ , also varies nonmonotonically with  $Ca$ .  $A_w$  reaches a minimum when a connected branched pattern forms (regime  $C$ ), and a maximum when the dendritic patterns form (regime  $D$ ).

The three transitions are clearly visible when inspecting the distribution of the water-film thickness  $P(h)$  and the non-monotonic variations of  $\langle h \rangle$  in Figs. 1(d) and 1(e). At low  $Ca$  (regime  $A$ ), the distribution is bimodal: the global maximum is located at  $h = H$ , the mean height of the channels. A smaller peak also exists at  $h = 0$  and trivially corresponds to the boundaries of the imbibition pattern. The transition from regime  $A$  to regime  $B$  occurs when the most probable film thickness  $h_M$  [defined as the location of the maximum of  $P(h)$ ] jumps from  $h = H$  to  $h = 0$ , Figs. 1(d) and 1(e). The second transition from regimes  $B$  to  $C$  is also visible on  $P(h)$ . When the connected branched pattern forms, the thickness distribution is still peaked at  $h = 0$  but plateaus at intermediate  $h$  values. Finally, the increase of the mean thickness  $\langle h \rangle$  in Fig. 1(e) signals the onset of regime  $D$ . In this regime, the two low- $h$  peaks seen on  $P(h)$  reflect the difference between the thickness of the finger tips and the water films left upstream as observed in Hele-Shaw geometries [23].

Three comments are in order. First, the abrupt variations of these macroscopic observables confirm that the four imbibition regimes correspond to four distinct physical processes. Second, as demonstrated in the Supplemental Material, document [14], increasing the viscosity ratio  $M$  keeping  $Ca = 2.2 \times 10^{-4}$ , we observed the same transitions from regimes  $A$  to  $B$ , and  $B$  to  $C$ , with the same signature on the film-thickness distribution. This classification in four regimes extends that proposed in Ref. [11], where disorder and the radial variations of the local flow rate are likely to blur the transitions between regimes  $A$ ,  $B$ , and  $C$ .

We now single out the microscopic origin of these four regimes by investigating the imbibition dynamics at the pore scale as illustrated in Fig. 2(a) and the Supplemental Material, movie 2 [14].

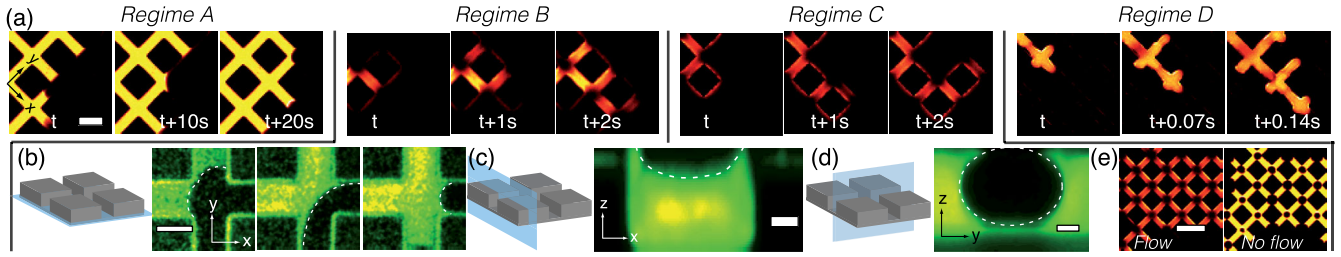


FIG. 2. (a) Consecutive snapshots of the interface dynamics at the pore scale in the four regimes. In regime *B*, the thin films are unstable, oil droplets form and are trapped at the vertices. In regime *C* the thin films are stable. Note the reversal of the apparent contact angle in regime *D*. Same capillary numbers as in Fig. 1(a). Scale bar:  $200\ \mu\text{m}$ . (b) Subsequent confocal images in the  $xy$  plane close to the sticker surface as indicated in the left panel. The contact line progresses everywhere past the sticker surface. Scale bar:  $100\ \mu\text{m}$ . (c) Confocal image of the cross section of a channel in regime *B*. Note that the water film is localized on the bottom surface, leaving an oil hemicylinder on the upper wall. Scale bar:  $20\ \mu\text{m}$ . (d) Same experiment imaged in the  $yz$  plane at the intersection between two channels: an oil droplet is trapped. Scale bar:  $20\ \mu\text{m}$ . (e) Destabilization of the thin films (regime *C*). Left picture: water flows and the films are stable ( $\text{Ca} = 2.2 \times 10^{-4}$ ). Right picture: the flow is stopped and the films are destabilized leaving oil droplets at the channel intersections. Scale bar:  $400\ \mu\text{m}$ .

*Regime A.*—Provides a prototypical illustration of cooperative pore filling [17]. The menisci proceed uniformly through the channels, merge at the vertices and grow until touching the next post. Then, they split into two interfaces invading the adjacent channels.

*Regimes B and C.*—Are associated with a marked change in the microscopic dynamics. As the contact line reaches a corner formed by a square post and a confining wall, the perimeter of the post is coated, leaving a significant fraction of oil immobile in the channels. The coating layer then grows, contacts adjacent posts, and discretely progresses through the lattice. This behavior is consistent with the strong imbibition scenario described by Zhao *et al.* in the high  $\text{Ca}$  limit; see Ref. [11]. Confocal imaging is, however, necessary to complete this scenario. The confocal pictures in Fig. 2(b) are taken  $5\ \mu\text{m}$  above the bottom surface of the channel (sticker surface). The progression of the water-oil interface in this plane is surprisingly similar to the sequences illustrating regime *A* in Fig. 2(a). Even though the contact line accelerates when reaching a corner, it also freely advances away from the posts along the direction of the microchannels. The advancing of the water film does not require any additional Laplace-pressure pumping from the negatively curved gutters at the base of the wetted posts [24]. A possible explanation could be the existence of a rough structure further driving the imbibition process at the suboptical scales [3]. This hypothesis is ruled out by atomic force microscopy imaging. Both the quartz and sticker surfaces are smooth down to the  $10\ \text{nm}$  scale [14]. Therefore, the only possible reason for the formation of a thin film in regimes *B* and *C* is a dynamical wetting transition akin to that discussed in Refs. [9,25]. The confocal image in the  $xz$  plane indeed shows that water films are entrained only on the bottom surface and fully cover it as they grow, Fig. 2(c) and the Supplemental Material, movie 3 [14]. Increasing  $\text{Ca}$ , the contact line on the sticker surface entrains the aqueous liquid at higher speed than the

average liquid front, thereby preventing the steady motion of a stable meniscus. This observation agrees with experiments in simpler Hele-Shaw geometries [9]. Note that the lower advancing contact angles on the sticker is very likely to trigger liquid entrainment on this surface first.

The dynamics of the water front are identical in regimes *B* and *C*. However, an interfacial instability distinguishes these two regimes, corresponding to different film thickness distributions in Fig. 1(d). In both cases, the incomplete displacement of the nonwetting fluid results in the formation of hemicylindrical interfaces as shown in Fig. 2(c). In regime *B*, these interfaces are unstable to the Rayleigh-Plateau instability: the oil threads break into droplets receding to the vertices of the lattice, Figs. 2(a) and 2(d). We stress that this instability does not rely on the contact-angle difference between the two surfaces, as in a homogeneous device the interfaces would still have a cylindrical shape. Increasing the flow rate to regime *C*, the Rayleigh-Plateau instability is suppressed. In principle, the stabilization of the oil hemicylinders could be either due to local pinning of the contact line [26,27], or by the convection of the interface fluctuations as in quickly stretched liquid filaments [28], and in coflowing liquid streams [29]. We single out the origin of this stabilization thanks to additional experiments started deep in regime *C* ( $\text{Ca} = 2.2 \times 10^{-4}$ ) and followed by an abrupt stop of the water flow illustrated in Fig. 2(e) and the Supplemental Material, movie 4 [14]. As the flow stops, the interfaces become unstable: the snap-off events and the resulting droplet pattern typical of regime *B* are recovered. This observation unambiguously confirms that the oil interfaces are dynamically stabilized by the flows in the water films.

*Regime D.*—The discontinuous variations of  $S_w$  and  $A_w$  at the onset of regime *D*, translate a marked qualitative change in the local meniscus dynamics. Given the speed of the water front, confocal imaging is no longer possible. However, it is already clear from the high-resolution

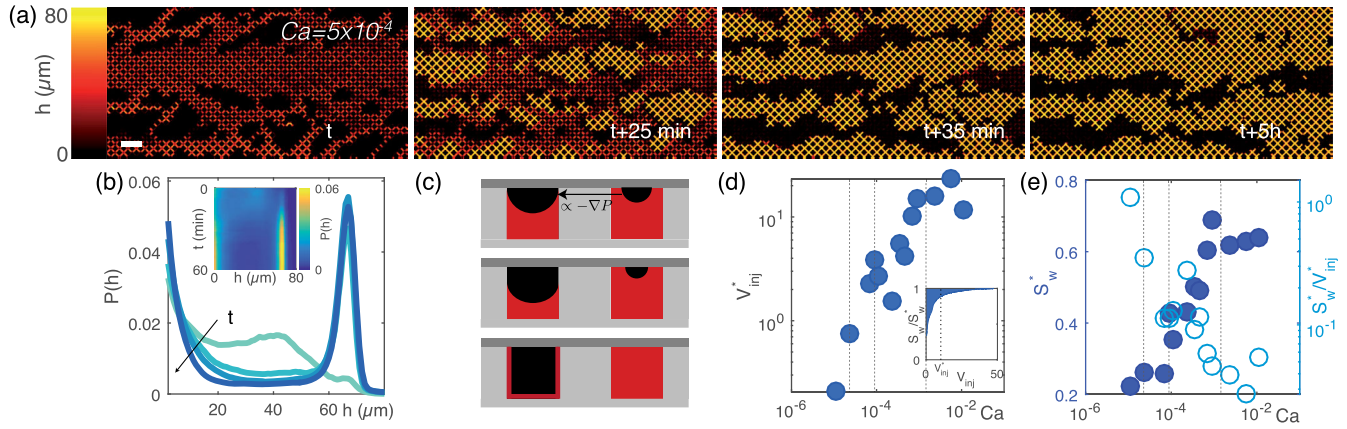


FIG. 3. Coarsening dynamics. (a) Snapshot of the imbibition films in regime *C*, where the color indicates the local height of the water films. The first snapshot is taken when water percolates through the lattice,  $t \sim 150$  s after injection. The thin films coarsen.  $Ca = 5 \times 10^{-4}$ ,  $M = 560$ , scale bar: 1 mm. (b) Distribution of the water-film thickness at times corresponding to the snapshots shown in (a). Inset: full temporal evolution of the film-thickness distribution. (c) Sketch of the coarsening mechanism. Oil flows from the regions of highest Laplace pressure. Equivalently, mass conservation implies that the thinner water films empty in the thicker. (d) Variation of  $V_{inj}^*$  with the capillary number. Inset: Measure of  $V_{inj}^*$ . The typical injection volume to reach a steady state corresponds to the area above the curve  $S_w(V_{inj})/S_w^*$ . (e) Opposite variations of  $S_w^*$  and  $S_w^*/V_{inj}^*$  with the capillary number.

snapshots in Fig. 2(a) that the apparent contact angle between the aqueous liquid and the solid walls is reversed: the porous medium becomes effectively hydrophobic. This apparent reversal is explained by another wetting transition first reported for immiscible colloidal liquids with ultralow surface tension [23]. In this high- $Ca$  regime, interface destabilization occurs at the center of the channels where a finger of the aqueous liquid grows and leaves an immobile oil layer on the solid surfaces. In turn, the lubricated motion of the water fingers becomes effectively analogous to a draingange dynamics at the pore scale. Hence, the imbibition patterns become analogous to dendritic growth as observed in conventional anisotropic drainage experiments [20–22].

In line with earlier studies, until now we have limited our discussion to pattern formation prior to the percolation of the driving fluid. This limitation is unimportant when liquid mobilization is achieved by the motion of a stable meniscus at the pore scale. Both in drainage experiments and in regime *A*, the driving fluid merely flows through a static percolating pattern [3]. In contrast, the thin-film patterns seen in regimes *C* and *D* undergo significant structural changes over long time scales. Figure 3(a) and the Supplemental Material, movie 5 [14] show the evolution of the film-thickness distribution over hours of continuous injection in regime *C* ( $Ca = 5 \times 10^{-4}$ ). From now on time is measured in terms of the volume of injected water normalized by the overall volume of the porous medium:  $V_{inj} = Qt/V_{Total}$ , in Fig. 3(a), the pattern percolates when  $V_{inj} = 0.27$ . Further increasing the injected volume, the oil-water interfaces are not destabilized by the Rayleigh-Plateau instability. Instead, the wetting pattern slowly evolves into compact islands of pores fully filled with water and connected by a sea of thin

films, Fig. 3(a). The islands grow at the expense of the thin films and eventually coalesce into a percolating cluster of pores where oil has been fully displaced. More quantitatively, we show in Figs. 3(b) [and 3(b) inset] that the water-thickness distribution evolves from a decreasing function to a bimodal distribution peaked both at  $h = 0$  (pattern edges and residual thin films) and  $h = H = 70 \mu\text{m}$  (filled channels). This slow dynamics has a clear microscopic origin. As sketched in Fig. 3(c), the curvature of the oil-water interface, and the resulting Laplace pressure, is smaller in the channels where the water films are thin. Therefore Laplace pressure gradients cause the oil to flow out of regions where the water films are thicker until total water saturation. This coarsening process relies on the capillary drive of the more viscous liquids which *de facto* results in a slower dynamics than the forced propagation of the water films. The collective relaxation of the  $h$  field further increases the volume of injected water needed to reach a stationary pattern. The typical water volume,  $V_{inj}^*$  required to reach the asymptotic steady state monotonically increases with  $Ca$  [see Fig. 3(d) and inset]: the higher the flow rate, the higher the water volume required to achieve maximal saturation and form stationary patterns. Unlike its value at percolation, the asymptotic value of  $S_w^*$  monotonically increases with  $Ca$ : pushing harder mobilizes more oil; see Fig. 3(e).

Altogether the variations of  $V_{inj}^*$  and  $S_w^*$  are useful guidelines to design optimal oil-recovery strategies. Decontamination processes requiring the mobilization of the maximal amount of oil, at any cost, would be optimized at the highest possible injection rate. Conversely, commercial oil extraction would require a trade-off, e.g., maximizing the  $S_w^*/V_{inj}^*$  ratio, which would correspond to minimizing the water flow rate, Fig. 3(e) (light circles).

From a more fundamental perspective, we hope our findings will stimulate experimental and theoretical investigation to quantitatively elucidate the interfacial instabilities underlying the fourfold dynamical scenarios established in this Letter.

We acknowledge support from Institut Universitaire de France (D. B.). We thank M. Faivre, C. Moscalenko, and M. Levant for help with the lithography, AFM, and SEM experiments. We also thank R. Juanes, G. McKinley, and especially A. Pahlavan for insightful comments and valuable suggestions.

---

\*Corresponding author.  
denis.bartolo@ens-lyon.fr

- [1] S. E. Buckley and M. C. Leverett, Mechanism of fluid displacement in sands, *Trans. Am. Inst. Mining and Metall. Engin.* **146**, 107 (1942).
- [2] R. Lenormand, E. Touboul, and C. Zarcone, Numerical models and experiments on immiscible displacements in porous media, *J. Fluid Mech.* **189**, 165 (1988).
- [3] R. Lenormand, Liquids in porous media, *J. Phys. Condens. Matter* **2**, SA79 (1990).
- [4] B. Sandnes, E. G. Flekkøy, H. A. Knudsen, K. J. Måløy, and H. See, Patterns and flow in frictional fluid dynamics, *Nat. Commun.* **2**, 288 (2011).
- [5] M. Sahimi, Flow phenomena in rocks: from continuum models to fractals, percolation, cellular automata, and simulated annealing, *Rev. Mod. Phys.* **65**, 1393 (1993).
- [6] M. Alava, M. Dube, and M. Rost, Imbibition in disordered media, *Adv. Phys.* **53**, 83 (2004).
- [7] J. P. Stokes, D. A. Weitz, J. P. Gollub, A. Dougherty, M. O. Robbins, P. M. Chaikin, and H. M. Lindsay, Interfacial Stability of Immiscible Displacement in a Porous Medium, *Phys. Rev. Lett.* **57**, 1718 (1986).
- [8] D. A. Weitz, J. P. Stokes, R. C. Ball, and A. P. Kushnick, Dynamic Capillary Pressure in Porous Media: Origin of the Viscous-Fingering Length Scale, *Phys. Rev. Lett.* **59**, 2967 (1987).
- [9] B. Levaché and D. Bartolo, Revisiting the Saffman-Taylor Experiment: Imbibition Patterns and Liquid-Entrainment Transitions, *Phys. Rev. Lett.* **113**, 044501 (2014).
- [10] J. S. Wexler, I. Jacobi, and H. A. Stone, Shear-Driven Failure of Liquid-Infused Surfaces, *Phys. Rev. Lett.* **114**, 168301 (2015).
- [11] B. Zhao, C. W. MacMinn, and R. Juanes, Wettability control on multiphase flow in patterned microfluidics, *Proc. Natl. Acad. Sci. U.S.A.* **113**, 10251 (2016).
- [12] M. Trojer, M. L. Szulczewski, and R. Juanes, Stabilizing Fluid-Fluid Displacements in Porous Media through Wettability Alteration, *Phys. Rev. Applied* **3**, 054008 (2015).
- [13] R. Holtzman and E. Segre, Wettability Stabilizes Fluid Invasion into Porous Media via Nonlocal, Cooperative Pore Filling, *Phys. Rev. Lett.* **115**, 164501 (2015).
- [14] See Supplemental Material at <http://link.aps.org/supplemental/10.1103/PhysRevLett.119.208005> where we report (i) a detailed description of the materials and methods, (ii) an AFM characterization of the surface roughness, and (iii) experiments performed at constant flow rate and increasing viscosity ratio.
- [15] D. Bartolo, G. Degre, P. Nghe, and V. Studer, Microfluidic stickers, *Lab Chip* **8**, 274 (2008).
- [16] B. Levache, A. Azioune, M. Bourrel, V. Studer, and D. Bartolo, Engineering the surface properties of microfluidic stickers, *Lab Chip* **12**, 3028 (2012).
- [17] M. Cieplak and M. O. Robbins, Mark, Influence of contact angle on quasistatic fluid invasion of porous media, *Phys. Rev. B* **41**, 11508 (1990).
- [18] L. Courbin, E. Denieul, E. Dressaire, M. Roper, A. Ajdari, and H. A. Stone, Imbibition by polygonal spreading on microdecorated surfaces, *Nat. Mater.* **6**, 661 (2007).
- [19] T. Cubaud and M. Fermigier, Faceted drops on heterogeneous surfaces, *Europhys. Lett.* **55**, 239 (2001).
- [20] J.-D. Chen and D. Wilkinson, Pore-Scale Viscous Fingering in Porous Media, *Phys. Rev. Lett.* **55**, 1892 (1985).
- [21] E. Ben-Jacob, R. Godbey, N. D. Goldenfeld, J. Koplik, H. Levine, T. Mueller, and L. M. Sander, Experimental Demonstration of the Role of Anisotropy in Interfacial Pattern Formation, *Phys. Rev. Lett.* **55**, 1315 (1985).
- [22] A. Budek, P. Garstecki, A. Samborski, and P. Szymczak, Thin-finger growth and droplet pinch-off in miscible and immiscible displacements in a periodic network of microfluidic channels, *Phys. Fluids* **27**, 112109 (2015).
- [23] S. A. Setu, I. Zacharoudiou, G. J. Davies, D. Bartolo, S. Moulinet, A. A. Louis, J. M. Yeomans, and D. G. A. L. Aarts, Viscous fingering at ultralow interfacial tension, *Soft Matter* **9**, 10599 (2013).
- [24] P. Concus and R. Finn, On the behavior of a capillary surface in a wedge, *Proc. Natl. Acad. Sci. U.S.A.* **63**, 292 (1969).
- [25] J. H. Snoeijer and B. Andreotti, Moving contact lines: Scales, regimes, and dynamical transitions, *Annu. Rev. Fluid Mech.* **45**, 269 (2013).
- [26] H. Gau, S. Herminghaus, P. Lenz, and R. Lipowsky, Liquid morphologies on structured surfaces: From microchannels to microchips, *Science* **283**, 46 (1999).
- [27] R. L. Speth and E. Lauga, Capillary instability on a hydrophilic stripe, *New J. Phys.* **11**, 075024 (2009).
- [28] S. Tomotika, Breaking up of a drop of viscous liquid immersed in another viscous fluid which is extending at a uniform rate, *Proc. R. Soc. A* **153**, 302 (1936).
- [29] J. Eggers and E. Villermaux, Physics of liquid jets, *Rep. Prog. Phys.* **71**, 036601 (2008).